Propagation of air fingers into an elastorigid Y-bifurcation

Haolin Li, Anne Juel, Finn Box, and Draga Pihler-Puzović*
Department of Physics and Astronomy and Manchester Centre for Nonlinear Dynamics, University of Manchester, Manchester M13 9PL, United Kingdom

(Received 11 July 2022; accepted 1 August 2023; published 5 September 2023)

We study experimentally the propagation of an air finger through the Y-bifurcation of an elastic, liquid-filled Hele-Shaw channel as a benchtop model of airway reopening. With channel compliance provided by an elastic upper boundary, we can impose collapsed channel configurations into which we inject air with constant volumetric flow rate. We typically observe steady finger propagation in the main channel, which is lost ahead of the Y-bifurcation but subsequently recovered in the daughter channels. At low levels of initial collapse, steady finger shapes and bubble pressure in the daughter channels map onto those in the main channel. However, at higher levels of initial collapse where the elastic sheet almost touches the bottom boundary of the channel, experimentally indistinguishable fingers in the main channel can lead to multiple states of reopening of the daughter channels. The downstream distance at which steady propagation is recovered in the daughter channels also varies considerably with injection flow rate and initial collapse because of a transition in the mechanics regulating finger propagation. We find that the characteristic time and length scales of this recovery are largest in the regime where viscous and surface tension forces dominate finger propagation and that they decrease towards a constant plateau in the limit where elastic forces supersede viscous forces. Our findings suggest that practical networks are unlikely to comprise long-enough channels for steady-state propagation to be recovered between bifurcations.

DOI: 10.1103/PhysRevFluids.8.094001

I. INTRODUCTION

Networks of elastic channels containing low-Reynolds-number multiphase flows are abundant in the human body. Compliance of these channels and ensuing interaction between fluids and elastic walls is a key feature of, e.g., the physiology of airways [1] and small blood vessels [2]. Often these vessels are collapsed, as in the case of bronchioles before pulmonary airway reopening, so that fluid flows in narrow gaps bounded by elastic walls [3]. Synthetic compliant networks are common in microfluidics where the interaction of a flow with an elastic component can introduce a functionality, such as a fluidic capacitance [4] or diodelike effect [5]. However, studies of channel networks with elastic components are still in their infancy.

Here we present an experimental study of two-phase flow through a Y-bifurcation in a rigid rectangular channel with an elastic upper boundary. Before the start of the experiment, the channel is completely filled with liquid which is then drained to induce deformation of the upper boundary.

*Corresponding author: draga.pihler-puzovic@manchester.ac.uk

Injection of air at constant volumetric flow rate reopens the initially collapsed channel via the propagation of an air finger. This type of elastorigid channel has been used previously as an idealized model of pulmonary airway reopening during the first breath of a newborn, when an air bubble reopens the strongly collapsed, branched airway network filled with liquid [6,7]. However, to our knowledge, this is the first attempt at studying experimentally the combined influence of channel bifurcation and elasticity in an airway reopening problem [8], although some attempts have been made to incorporate elastic elements into mostly rigid networks. For example, Baroud *et al.* [9] studied finger propagation through a rigid, microfluidic Y-channel and investigated the influence of elastic chambers attached to the ends of the daughter channels. Asymmetric branching of the main finger was systematically observed when the identical daughter channels had open ends. However, when the daughter channels were each connected to a large elastic chamber, identical fingers propagated through both daughter channels for sufficiently small propagation speeds.

Our study will tackle two questions associated with fluid flows in networks: (i) how symmetric is the flow after it encounters a channel bifurcation and (ii) how it recovers postbifurcation. The question of flow symmetry through different network pathways is of fundamental importance for studying airway reopening. It is also pertinent to transport of bubbles, droplets, capsules, and other cargo passing through bifurcations in, e.g., microfluidics [10]. For example, bifurcation-induced deformation of red blood cells flowing through a microfluidic network in a dilute suspension has no time to relax before the next fork in the network is encountered, which directly impacts the cell distribution at the network scale [11]. Here we consider a different type of compliant system and focus on one bifurcation as a building block towards multigenerational branching networks.

So far, however, most theoretical and experimental works on airway reopening have focused on a single initially collapsed fluid-filled tube or compliant channel, reopened by the propagation of an injected air finger which redistributes the resident fluid. Early theoretical works [12–15] systematically reported two branches of solution in terms of finger pressure P and capillary number $\mathrm{Ca} = \frac{\mu U}{\sigma}$, where U is the finger tip speed and μ and σ are fluid viscosity and surface tension, respectively. The level of collapse sets the pleural pressure (i.e., the pressure downstream), so in the context of pulmonary mechanics, the results are often reported in terms of the pressure difference between the bubble pressure and the pleural pressure. The two branches meet at a limit point associated with a minimum pressure difference or yield pressure difference, which needs to be exceeded for steady propagation to occur. Above this yield pressure difference, two distinct behaviors are observed: pushing at low Ca, for which P decreases with increasing Ca, and peeling at high Ca, for which P increases with increasing Ca [13]. Furthermore, the pushing branch was found to be linearly unstable in a two-dimensional (2D) geometry consisting of a layer of liquid trapped between infinite, planar, elastic walls [15]. Hence, stable reopening only took place via peeling solutions. However, despite revealing some of the fundamental dynamics of the reopening process, these early models were idealized: The 2D models of Gaver *et al.* [13], Jensen *et al.* [14], Halpern *et al.* [15] could not capture the in-plane finger shape because of its unbounded geometry, while the three-dimensional steady simulations of Hazel and Heil [12] imposed symmetry about the two longitudinal midplanes of the tube, thus eliminating a host of asymmetric solutions observed experimentally [16].

Early experimental studies of airway reopening reported a single peeling branch for different oil-filled realizations of quasi-2D geometries and identified the yield pressure difference, which occurs for vanishingly small values of Ca in the presence of gravity [17–20]. However, it is now well established that tubes can be reopened by a variety of different propagation modes. In their experiments, Heap and Juel [16] studied tubes that were strongly collapsed into two-lobed cross sections and revealed reopening characterized by round-, asymmetric-, double-, and pointed-tipped finger shapes, with P increasing with Ca in all experiments. They also reported that at a critical value of Ca, a discontinuous drop in bubble pressure was accompanied by a transition from double- to pointed-tipped finger shapes, suggesting that the system had at least two discontinuous peeling branches of reopening. Ducloué *et al.* [6] explored reopening of a rectangular elastorigid channel of

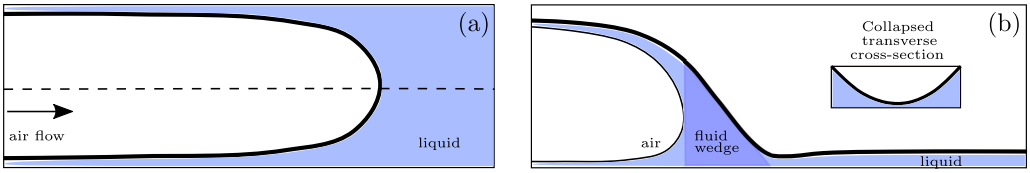

FIG. 1. Schematic diagram of reopening of a liquid-filled elastorigid channel by an air finger: (a) top view and (b) side view along the channel centerline shown with dashed line in (a). The inset in (b) shows schematically a collapsed transverse cross section of the channel at the start of experiment, which is maintained sufficiently far ahead of the interface (i.e., beyond the "fluid wedge" region) throughout the reopening experiment.

large aspect ratio (a Hele-Shaw channel), shown schematically in Fig. 1, and found that this simpler quasi-2D geometry exhibits similar physics of reopening as observed in collapsible tubes.

The injection of air into an analogous liquid-filled rigid-walled channel of rectangular cross section gives rise to the classical Saffman-Taylor instability, which typically results in the steady propagation of a symmetric round-tipped finger [21]. This displacement flow is governed by the ratio between viscous and surface tension forces measured by Ca and it can also exhibit complex behaviors associated with, for example, geometric perturbations to the channel geometry [22–24]. In elastorigid channels, air injection induces elastic deformation in addition to viscous and surface tension forces, and this alters the two-phase flow fundamentally. Rather than displacing fluid, the propagating air finger, seen in top view in Fig. 1(a), tends to inflate the channel and redistributes fluid within a wedge ahead of its tip as shown in Fig. 1(b). This wedge is relatively long at lower levels of initial collapse and small Ca, and Ducloué *et al.* [6] found that symmetric fingers analogous to the Saffman-Taylor finger propagate in the channel. However, as the amount of fluid contained within the liquid wedge reduces with increasing initial collapse and/or Ca, fingers of different morphology can form [6,25]. Longer liquid wedges are associated with dominant balance between viscous and surface tension forces (this regime is referred to as "viscous"), while shorter liquid wedges are linked to elastic forces superseding viscous forces (this regime is referred to as "elastic") [25]. As the reopening transitions from viscous to elastic, fingers start penetrating the shallowest parts of the channel and peeling them apart much like in the classical problem of the peeling of a flexible strip [26,27]. Furthermore, their fronts become flatter and prone to interfacial instabilities [22,28,29], leading to more exotic shapes of reopening fingers such as, e.g., feathered fingers, whose front perturbations are advected away from the tip along trajectories instantaneously normal to the curved interface [30]. Many experimental results were reproduced quantitatively in recent quasi-2D models [31,32]. They showed that diversity of propagation modes are associated with complex solution structure with a wide range of stable and unstable, steady and time-periodic modes, many occurring at similar values of the driving pressure. Most notably, a parameter regime existed in which, depending on initial conditions, the elastorigid channel could be reopened by a bubble propagating with different Ca for the same values of the bubble pressure [25]. Significance of unsteady reopening was also corroborated by long-lived transients.

Given that unsteady reopening is common in a rectangular elastorigid channel with high level of initial collapse [31,32], it is also likely to be a feature of the bubble propagation in a network of elastic channels. However, in theoretical models of reopening of a network of occluded airways, only steady reopening is assumed to take place and only if the bubble pressure exceeds a critical threshold dependent on material parameters [33,34] in line with early studies of reopening by Hazel and Heil [12] and Halpern *et al.* [15]. Yamaguchi *et al.* [35] found similarities in the reopening of a rigid Y-channel in the presence of surfactants with reopening of a rigid Y-channel connected to an elastic end chamber in Ref. [9], implying that wall elasticity is also likely to be of fundamental importance in the related problem of liquid plug propagation in airways. However, this phenomenon is typically investigated using rigid branching channels [36–38], in which the physics is described

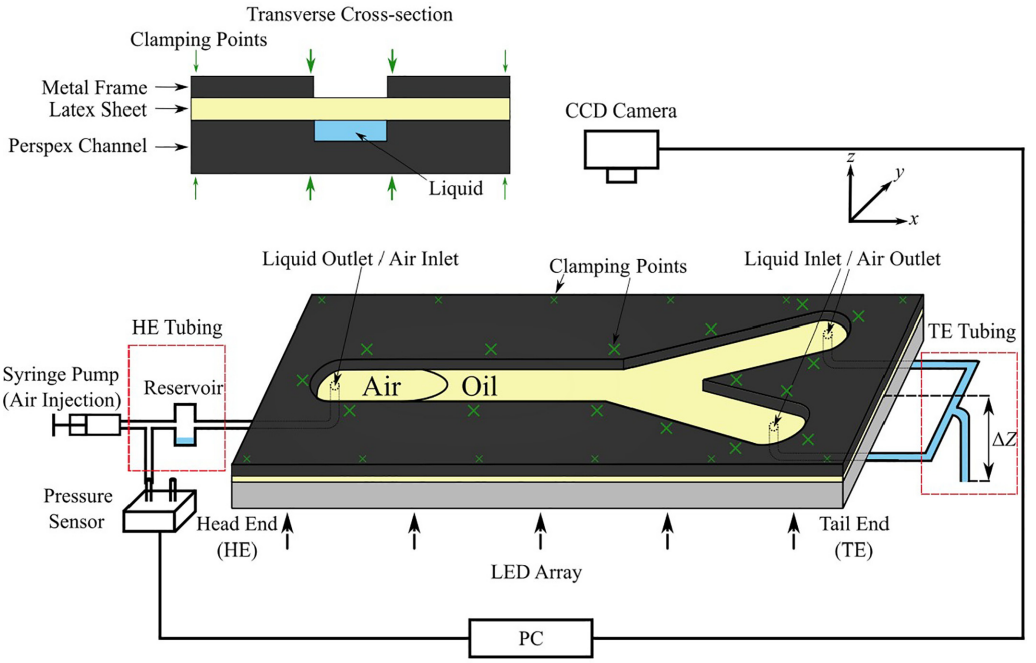

FIG. 2. Schematic diagram of the experimental setup.

by relating the driving pressure head to the flow resistance caused by the viscous dissipation and capillarity. These can be written down accurately for each network generation if its geometry is known, but we are yet to build rational lower-dimensional models in which the network geometry can evolve in response to the changing fluid resistance as in elastic-walled channels.

In this paper, we explore experimentally the transfer of reopening modes between the channels upstream and downstream of the elastorigid Y-bifurcation at various levels of initial collapse and injection rates. Our experimental setup and methods are introduced in Sec. II. In Sec. III A, we show that steady modes of finger propagation upstream of the Y-bifurcation transfer to different steady modes expected for suitably reduced flow rates downstream of the Y-bifurcation. However, in the limit of large initial channel collapse multiple reopening modes can coexist downstream of the Y-bifurcation, and we explore this regime further in Sec. III B. We also find that transient evolution of reopening fingers downstream of the Y-bifurcation typically persists over a significant distance before they recover a state of steady propagation. Hence, in Sec. III C we study the unsteady finger propagation through the Y-bifurcation, relating the time- and length scales for fingers to recover steady states in the daughter channels to the reopening dynamics. In Sec. IV, we conclude that simple transfer scenarios through the Y-bifurcation can only be assumed for sufficiently long channels and only in the regimes without finger multiplicity.

II. EXPERIMENTAL METHODS

The experimental setup, a Y-shaped elastorigid Hele-Shaw channel with a flexible upper boundary, is shown schematically in Fig. 2. It consists of three regions: a main channel, two daughter channels, and a bifurcation region, where the two daughter channels meet [see Fig. 3(a)]. The Y-shaped channel of constant depth $b = 0.5 \pm 0.01$ mm was milled into a transparent Perspex block by cutting a rectangular channel of length 483 ± 0.02 mm and width $W = 15 \pm 0.02$ mm, and two rectangular channels of length 310 ± 0.02 mm and the same width W as the first channel, oriented at $\pm 30^\circ$ to the center line of the main channel. The Perspex block was covered by a rectangular latex

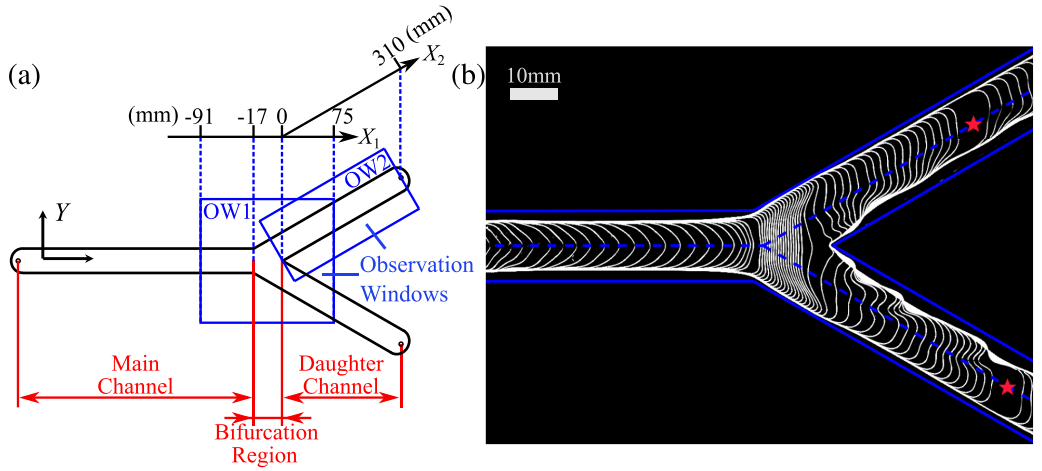

FIG. 3. (a) Schematic diagram of different regions in the Y-channel. X_1 and X_2 axis are aligned with the centerlines of the main and daughter channels, respectively, and the Y axis is perpendicular to X_1, so that the apex of the bifurcation is at $X_1 = X_2 = Y = 0$. The channel width in the bifurcation region of length 17 ± 0.02 mm varies linearly between 15 ± 0.02 mm and 34.64 ± 0.02 mm. (b) Typical spatiotemporal composite image of the bifurcation region, obtained for $A_i = 0.36$ in the main channel and $Q = 50$ ml/min. The time interval between sequential contours is 0.033 s. The blue solid and dashed lines denote the boundaries and the central lines of the main or daughter channels, respectively. In (b), one frame is lost during recording, so the position of the missing contour is marked with a red star.

membrane (Supatex) of thickness 0.33 ± 0.01 mm, Young's modulus $E = 1.44 \pm 0.05$ MPa, and Poisson's ratio $\nu = 0.5$ [28]. The membrane was stretched uniformly in the direction transverse to the main channel and clamped using a metal frame and G-clamps to form the upper boundary of the Y-shaped channel [6,25]. Uniform transverse prestress was achieved by hanging evenly distributed weights of total mass 2.49 ± 0.01 kg onto the membrane along one of the long edges of the Perspex block before clamping, resulting in pretension of 32.5 N/m applied parallel to the width of the main channel, and zero pretension parallel to the centerline of the main channel.

Prior to each experiment, the channel was completely filled with silicone oil (Basildon Chemical Company Ltd.) of viscosity $\mu = 0.019$ Pa s, density $\rho = 953$ kg m^{-3}, and surface tension $\sigma = 20.8$ mN m^{-1} at temperature $T = 21 \pm 1$°C. The liquid or gas was supplied to or evacuated from the system using ports at the channel ends connected to tubing, and referred to as the head end (HE) and the tail end (TE) in Fig. 2. During the filling procedure, some of the liquid drained from the main channel into the HE tubing, so a reservoir was added halfway along it to trap excess liquid. This avoided the obstruction of the air line with silicone oil. With the HE closed, the channel was collapsed by setting a hydrostatic pressure difference P_h between the channel and ambient laboratory pressure at the TE. The pressure difference caused the membrane to collapse symmetrically with respect to the vertical midplane of the channel and uniformly along most of its length (see Fig. 4).

The reopening experiments were performed by injecting air into the fluid-filled channel using a syringe pump (KDS 210) with a constant volumetric flow rate Q set between 10 ml/min and 150 ml/min. The resulting propagation of an air finger within the Y-shaped channel was captured in two observation windows with top-view CMOS cameras (Teledyne Dalsa CR-GM00-H1400, resolution 1400×1024 pixels) at 60 frames per second. To improve image quality, the channel was lit from below by a custom-built LED array. The image resolution was 0.117 mm/pixel in the first observation window (OW1), which covers the main channel, the bifurcation region and the upstream end of the daughter channels, and 0.224 mm/pixel in the second observation window (OW2), which covers just one of the daughter channels [see Fig. 3(a)]. The images were processed

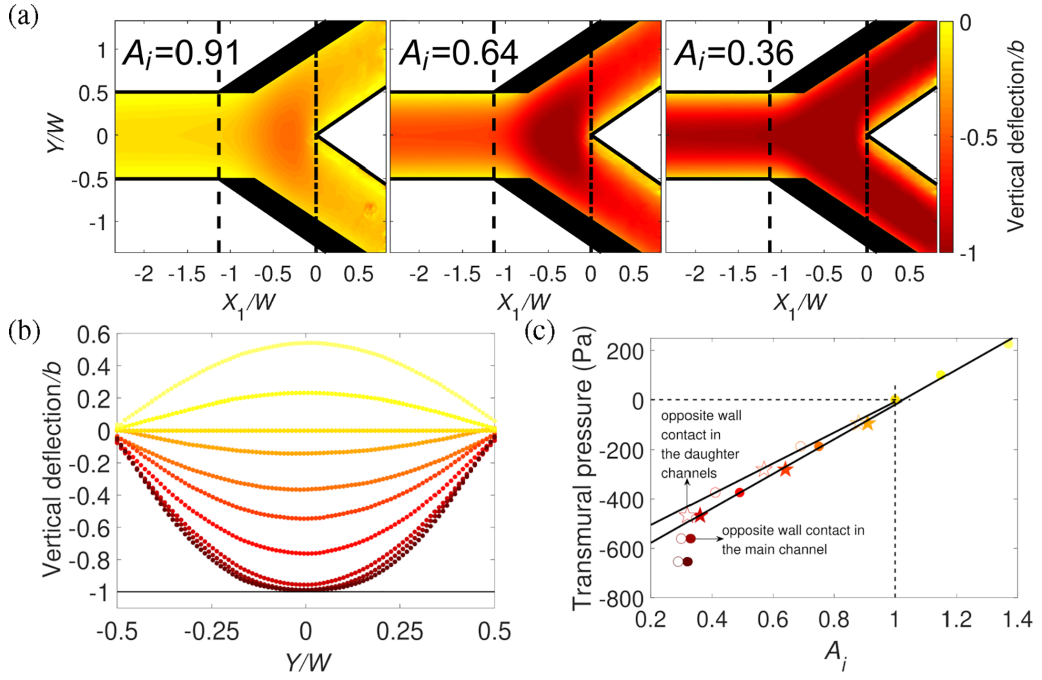

FIG. 4. (a) Membrane profiles for $A_i = 0.91$, 0.64, and 0.36 in the main channel (left to right) before the start of air injection with color-coding corresponding to the vertical deformation of the membrane scaled by b. Regions of the channel, where the vertical deformation could not be reconstructed, are black (for details, see Appendix A). Lines denote the boundaries of the channel (solid lines), the start of bifurcation region (vertical dashed line), and the apex of the bifurcation (vertical dash-dotted line). (b) Transverse profiles of the membrane at $X_1/W = -2$ for $A_i = 1.37$, 1.15, 1, 0.91, 0.75, 0.64, 0.49, 0.36, 0.33, and 0.32 (top to bottom) before the air injection starts. (c) Transmural pressure across the membrane as a function of the level of initial collapse A_i in the main (filled markers) and daughter (empty markers) channels, with zero transmural pressure corresponding to no membrane deflection ($A_i = 1$). Lines are linear fits to the experimental data above the points of the opposite wall contact. Star markers are used for the levels of collapse which correspond to the membrane profiles in (a) and are referred to as low [$A_i = 0.91$ (0.88) in the main (daughter) channel], moderate [$A_i = 0.64$ (0.57) in the main (daughter) channel], and high [$A_i = 0.36$ (0.32) in the main (daughter) channel] initial collapse in the paper, respectively. The colors in (b) and (c) are consistent.

in MATLAB to create spatiotemporal composite images, such as in Fig. 3(b). During the longer recordings, occasional frames were lost due to technical limitations of the imaging hardware. The spatiotemporal patterns enabled us to study finger evolution and extract, for example, the finger speed and tip position. The finger pressure P (relative to atmospheric pressure) was measured with a pressure sensor (Honeywell 163PC01D36 $\pm$ 5″ H_2O) inserted into the middle of the air supply line using a T-shaped tubing adapter, taking care to subtract the small pressure losses in the line.

The time evolution of the membrane deformation during reopening experiments was reconstructed using a custom-built digital-image-correlation technique, described in detail in Appendix A. Examples of collapsed membrane profiles before the start of air injection are shown in Fig. 4(a). These results indicate that for each value of P_h, the initial level of collapse differs in different regions of the Y-channel because of its varying geometry. For example, opposite wall contact, in which the thickness of the liquid film between the membrane and the channel becomes smaller than our experimental resolution, first occurs in the bifurcation region where the channel is the widest and thus has the smallest effective stiffness [39]. The level of initial collapse is reported using the nondimensional cross-sectional area $A_i = A_t/A_0$ measured at $X_1/W = -2$ in the main channel

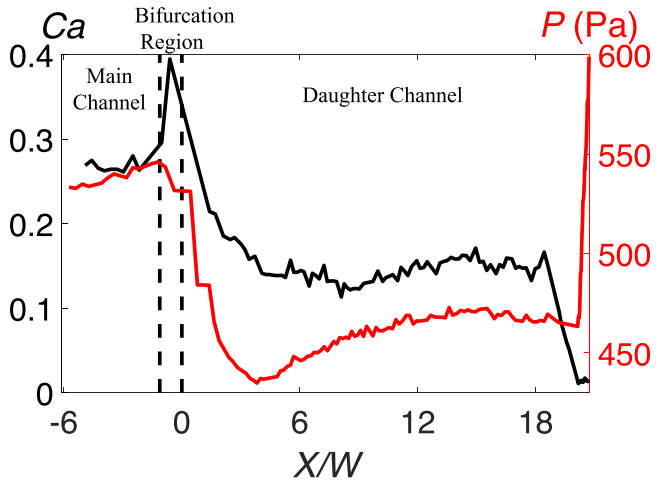

FIG. 5. Ca (black line) and P (red line) as a function of scaled finger tip position X/W ($X = X_1 \cup X_2$) for $A_i = 0.91$ (0.88) in the main (daughter) channel and $Q = 150$ ml/min. Vertical dashed lines delineate different regions in the Y-channel.

and at $X_2/W = 0.67$ in the daughter channels, respectively, where A_t and A_0 denote the collapsed and undeformed transverse cross-sectional areas, respectively, so that $A_t/A_0 = 1$ corresponds to a channel with a rectangular cross section.

Examples of membrane profiles in the cross section of the main channel, which are used for estimating A_i, are shown in Fig. 4(b) for a range of transmural pressures (i.e., the difference between internal and external pressure). The shape of the channel is symmetric with respect to its centerline where the deflection is maximum. The channel is inflated under positive transmural pressure ($A_t/A_0 > 1$) and collapsed under negative transmural pressure ($A_t/A_0 < 1$). The same data are presented differently in Fig. 4(c), where transmural pressure is shown as a function of initial level of collapse for the main and the daughter channels, respectively. It demonstrates that for a fixed value of transmural pressure, the daughter channels are more collapsed (i.e., have a smaller A_i) than the main channel. This is because the prestretch is applied in the direction parallel to the width of the main channel and thus obliquely to the daughter channels, which means that the daughter channels have a smaller effective stiffness. Based on estimates using the finite number of points in Fig. 4(c), the first opposite wall contact in the main channel occurs at $A_i = 0.33$, whereas it is already seen in the daughter channels at $A_i = 0.36$. In the vicinity of those points, small changes in A_i result in large pressure variations in the main and daughter channels, respectively. However, for the data above the points of opposite wall contact in Fig. 4(c), the transmural pressure increases linearly with A_i. In this paper, we mostly report experiments at $A_i = 0.91$, 0.64, and 0.36 in the main channel and refer to these levels of initial collapse as low, moderate, and high, respectively. The corresponding A_i in the daughter channels were 0.88, 0.57, and 0.32, respectively, and we stress the difference between the initial cross-sectional areas in different parts of the Y-channel where required. To achieve these levels of collapse, we set P_h to -93, -280, and -467 Pa, respectively.

III. RESULTS

We performed reopening experiments in our Y-shaped channel under low, moderate, and high levels of initial collapse (see Sec. II) for a wide range of constant volumetric air injection rates Q. Figure 5 shows typical traces of the dimensionless finger speed $\mathrm{Ca} = \frac{\mu U}{\sigma}$ (black line), where U is the finger tip speed, and bubble pressure P (red line) as a function of the position of the finger tip X normalized by the channel width W. This finger tip coordinate is aligned in turn with the main

and daughter channels as the air finger propagates through the Y-shaped channel. The pressure is approximately constant to within the experimental resolution of 5 Pa in the main channel. This indicates a steady mode of finger propagation, which exhibits an approximately constant Ca. The varying channel geometry around the Y-bifurcation leads to nonmonotonic variations of Ca and P as the finger tip approaches and propagates through the bifurcation region. The main finger splits at the Y-bifurcation into two propagating daughter fingers with the same pressure P and individually measured values of Ca. As they propagate through the daughter channels, their typical evolution is towards a steadily propagating finger. In the experiment shown in Fig. 5, both P and Ca exhibit measurable variations in the first half of the daughter channel, only reaching constant values for $X_2/W \approx 12$. Once the steady state is reached in the daughter channel, the finger propagates with a value of Ca that is approximately half of that in the main channel. This is because the flow rate divides equally between the identical daughter channels, which have very similar cross sections to the main channel, and the relationship between flow rate and Ca is approximately linear [32]. The steady-state pressure is accordingly reduced in the daughter channels, compared to that of the main channel.

Our experiments also showed a small, systematic bias that promoted finger propagation in one daughter channel ahead of the other upon exit from the Y-bifurcation. However, once steady propagation was recovered, the relative position of the two finger tips did not change. This is dramatically different from behavior expected in an analogous rigid system, in which the difference between the two daughter fingers would continue to increase because the finger closer to the channel end would experience a larger pressure gradient [9]. Naturally, the leading daughter finger in the elastic-walled channel reached its end before the trailing finger. Fluid ahead of the leading finger was displaced into the rigid outlet tubing, increasing resistance to air propagation. This led to a sharp increase of P and the abrupt reduction of the velocity of the trailing finger (at $X_2/W \approx 18.4$) seen in Fig. 5. The distance from this point to the end of the daughter channel gives the relative distance between the tips of the leading and trailing daughter fingers in steady propagation. Although this distance varied with flow parameters, it remained systematically smaller than two channel widths and did not measurably influence the dynamics. Thus, we do not mention this bias henceforth.

We begin in Sec. III A by examining how steady modes of finger propagation transfer from the main channel to the daughter channels. We discuss the multiple modes of propagation encountered as a function of A_i and Ca by comparison with previous studies in straight elastorigid Hele-Shaw channels [6,25,31,32]. We show in Sec. III B that for high collapse, reopening modes in the main channel can transfer to multiple outcomes in the daughter channels. We then proceed in Sec. III C to characterize the recovery of steady finger propagation in the daughter channels.

A. Steadily propagating fingers in the main and daughter channels

We found that fingers propagate steadily through the main channel for most of the parameters investigated. Their pressure, averaged over the domain $-3.5 < X_1/W < -2.5$, is shown with circles in Fig. 6 as a function of the average capillary number $\overline{\mathrm{Ca}}$, for low, medium, and high initial collapse of the channel. The error bars on $\overline{P}$, which indicate standard deviation over the visualization domain, are always within ± 7 Pa and thus typically hidden by the markers. The largest pressure fluctuations were measured for fingers which failed to settle to a state of steady propagation and thus evolved continually over the visualization window. These experiments are shown with blue markers in Fig. 6. In contrast, the standard deviation of $\overline{\mathrm{Ca}}$ is not a good indicator of steady finger propagation. The corresponding error bars tend to increase as Ca or the level of initial collapse increases, because the liquid wedge ahead of the finger tip which sets the finger velocity becomes thinner and thus the finger becomes increasingly sensitive to channel imperfections [25,29].

Stars indicate fingers propagating in the daughter channels, which are shifted to approximately half the value of $\overline{\mathrm{Ca}}$ in the main channel because the flow divides equally between the two daughter channels. The color of the markers is used to identify fingers in the main and daughter channels

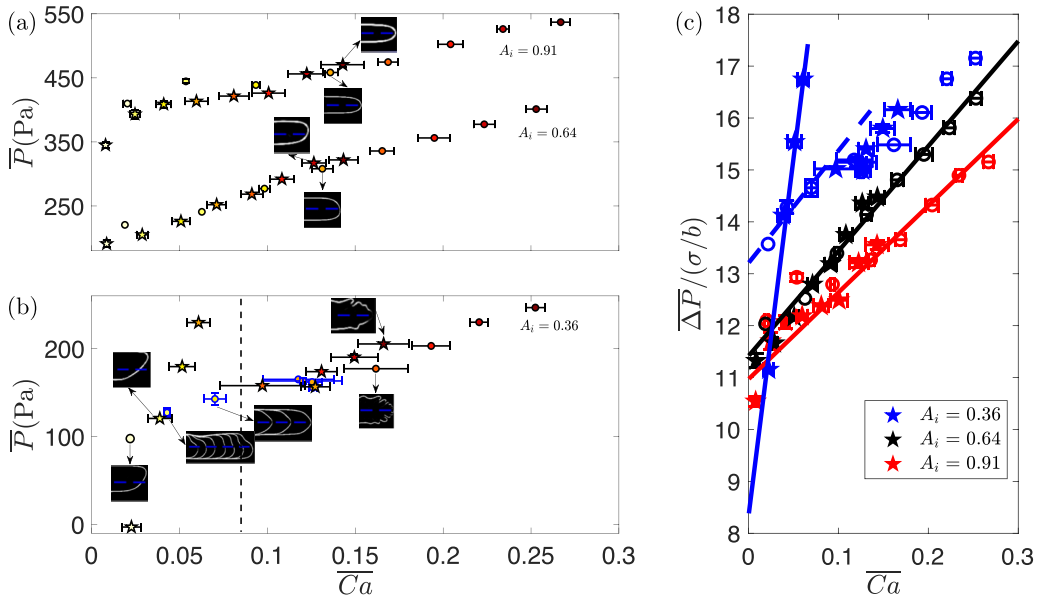

FIG. 6. [(a) and (b)] Averaged finger pressure $\overline{P}$ as a function of averaged capillary number $\overline{\mathrm{Ca}}$ for different levels of initial collapse: (a) $A_i = 0.91/0.88$ and $A_i = 0.64/0.57$ and (b) $A_i = 0.36/0.32$ in the main channel (circles) and the daughter channels (stars), respectively. The data for the main and the daughter channels obtained in the same experiment are shown using the same colors. Markers with blue boundaries in (b) correspond to transiently evolving fingers with a nonconstant pressure trace throughout the main channel. The insets show typical fingering patterns (either steadily propagating or, when there is more than one contour, transiently evolving fingers) in different regions of the parameter space. The vertical line in (b), intended to guide the eye, separates the region of lower $\overline{\mathrm{Ca}}$, in which the difference between the data in the main and the daughter channels is the greatest. (c) Scaled pressure difference $\overline{\Delta P}/(\sigma/b)$, where $\overline{\Delta P} = \overline{P} - P_h$, as a function of averaged capillary number $\overline{\mathrm{Ca}}$ for all data from (a) and (b). The marker shapes are the same as in (a) and (b). The lines provide a guide to the eye for extrapolating the pressure difference to $\overline{\mathrm{Ca}} = 0$ for each peeling branch.

which originated from the same experiment. The length of the region where fingers propagate steadily depends on the length of transients but averages of $\overline{P}$ and $\overline{\mathrm{Ca}}$ are taken after the finger reaches steady propagation (see Sec. III C).

Results shown in Fig. 6 are consistent with previous studies in nonbranching channels, with small quantitative differences originating in variations of the constitutive relationships between pressure and cross-sectional area of the channels [25,31,32]. In all experiments, the finger pressure increases with $\overline{\mathrm{Ca}}$, which indicates reopening via the propagation of peeling fingers [13]. In Fig. 6(a), which shows results for low and medium levels of initial collapse, circles and stars follow similar trends, indicating that the reopening dynamics are insensitive to the difference of up to 11% between the initial level of collapse in the main and daughter channels (see Sec. II). This is confirmed by the inset images of matching fingers from the main and daughter channels at the same values of $\overline{\mathrm{Ca}}$. The same data are shown in Fig. 6(c), where we relate the pressure difference $\overline{\Delta P} = \overline{P} - P_h$, normalized by the capillary pressure scale σ/b, to the capillary number $\overline{\mathrm{Ca}}$ for various levels of initial collapse. Estimating $\overline{\Delta P}$ at $\overline{\mathrm{Ca}} = 0$ for the two peeling branches in Fig. 6(a) shows that the corresponding yield pressure differences are approximately the same, $\overline{\Delta P}(\overline{\mathrm{Ca}} = 0) \approx 11\sigma/b$, despite the significant differences in the magnitude of $\overline{P}$ between the branches.

For low and medium levels of initial collapse in our experiments, the fingers are round-tipped, see Fig. 6(a). They are associated with a relatively long liquid wedge ahead of them, so that the

dominant force balance is between viscous and surface tension forces. At $A_i = 0.91$ (0.88) in the main (daughter) channel, the fingers are symmetric about the centerline of the channel. When $A_i = 0.64$ (0.57) in the main (daughter) channel, the fingers become increasingly asymmetric about the centerline of the channel with increasing $\overline{\mathrm{Ca}}$. As explained Ref. [6], the finger asymmetry at moderate levels of collapse stems from more significant variations of the liquid thickness within the transverse cross section of the channel: The maximum collapse of the membrane occurs along the centerline of the channel, with deflection reducing to zero near its boundaries where the sheet is clamped [see Fig. 4(b)]. This promotes reopening with fingers propagating closer to one of the channel side walls where the viscous resistance is smaller.

We observed more complex dynamics for high initial collapse [Fig. 6(b)] consistent with previous findings [25,31,32]. In the main channel ($A_i = 0.36$), a succession of different modes of finger propagation was observed for increasing $\overline{\mathrm{Ca}}$, including asymmetric, asymmetric with intermittent tip perturbations, pointed-tipped fingers and feathered patterns, where small-amplitude viscous fingering occurs at the bubble tip. The appearance of feathered patterns has been associated with a switch from viscous forces to elastic forces balancing surfaces tension forces in the reopening process. Figure 6(b) also shows that the dynamics at high initial collapse (i.e., close to the point of the opposite wall contact) is very sensitive to small changes of the initial cross-sectional area between the main and daughter channels. In the main channel, all the reopening fingers exhibit unsteady behavior in the vicinity of the vertical dashed line, indicating a region of complex dynamics. For $\overline{\mathrm{Ca}} \lesssim 0.09$ [left of the vertical dashed line in Fig. 6(b)], the finger pressure in the daughter channel increases steeply with increasing $\overline{\mathrm{Ca}}$ and does not map to the peeling curve measured for the main channel. Accordingly, the inset pictures captured in the main and daughter channels at approximately the same value of $\overline{\mathrm{Ca}}$ do not match like in Fig. 6(a). Thus, the corresponding yield pressure differences, estimated at $\overline{\mathrm{Ca}} = 0$ in Fig. 6(c), also differ considerably; we obtain $\overline{\Delta P}(\overline{\mathrm{Ca}} = 0) \approx 8\sigma/b$ and $\overline{\Delta P}(\overline{\mathrm{Ca}} = 0) \approx 13\sigma/b$ for the daughter and the main channels, respectively. However, these values remain of same order of magnitude as the values found in Refs. [17–19]. In contrast, for $\overline{\mathrm{Ca}} \gtrsim 0.09$ [right of the vertical dashed line in Fig. 6(b)], variations of $\overline{P}$ with $\overline{\mathrm{Ca}}$ in main and daughter channels are similar to each other. The data for the daughter channels clearly forms two disconnected branches of steadily propagating fingers on either side of the vertical dashed line. In the range $156 < \overline{P} < 231$ Pa, fingers with similar values of $\overline{P}$ can propagate in the daughter channels with different average dimensionless speeds $\overline{\mathrm{Ca}}$, indicating a region of bistability.

The existence of this region of bistability for the reopening of the Y-bifurcation is best illustrated by repeated experiments conducted at the flow rate $Q = 70$ ml/min. In these experiments, similar values of $\overline{P}$ and $\overline{\mathrm{Ca}}$ were recorded to within experimental resolution in the main channel. However, propagation of the fingers into the daughter channel led to distinct peeling behaviors in consecutive experiments resulting in data points on both sides of the dashed line in Fig. 6(b). We explore the sensitivity of the reopening modes of the Y-channel in further detail in the next section (Sec. III B.)

B. Multiple modes of finger propagation for the same injection rate

Figure 7(a) shows a close-up of $\overline{P}$-$\overline{\mathrm{Ca}}$ curve near the transition between two peeling branches from Fig. 6(b), highlighting a selection of data from 20 identical experiments at $Q = 70$ ml/min. In these experiments, fingers in the main channel largely resemble each other [Figs. 7(b)–7(d)], although the feathered pattern evolves within the visualization region in all experimental runs. For example, these fingers even briefly resemble the pointed-tipped symmetric fingers observed at lower values of $\overline{\mathrm{Ca}}$ [compare the red contours in Figs. 7(b)–7(d) to finger shapes in Fig. 6(b) at $\overline{\mathrm{Ca}} \approx 0.075$]. In contrast, three different modes of propagation, labeled M1, M2, and M3, are observed in the daughter channels [Figs. 7(e)–7(g)]. M1 and M2 correspond to asymmetric fingers and feathered fingering patterns, respectively. M3 fingers continually evolved throughout the daughter channel from (i) a feathered finger to (ii) a pointed-tipped finger and finally to (iii) an asymmetric finger. Remarkably, the two daughter channels could be either reopened by the same mode, e.g., M1 in

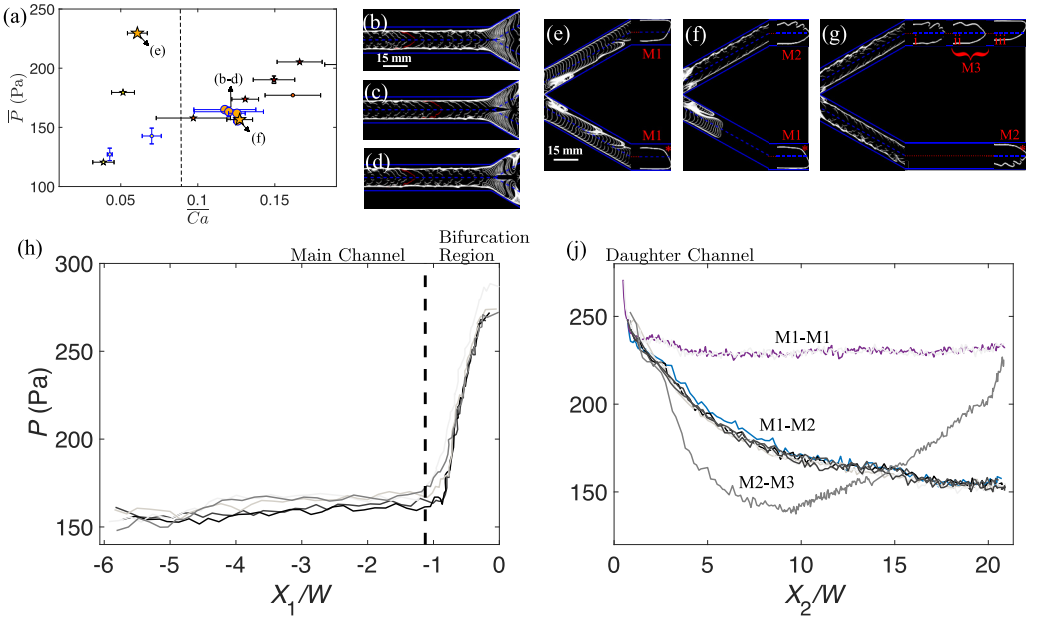

FIG. 7. (a) Averaged finger pressure $\overline{P}$ as a function of averaged capillary number $\overline{\mathrm{Ca}}$ from Fig. 6(b) zoomed in on the region of bistability. [The vertical dashed line in (a) is exactly analogous to the vertical dashed line in Fig. 6(b).] Larger markers highlight experiments shown in [(b)–(j)]. Superposition of sequential contours with time interval of 0.033 s during reopening of [(b)–(d)] the main channel, initially collapsed to $A_i = 0.36$, and [(e)–(g)] the daughter channels in the same experimental runs, respectively, initially collapsed to $A_i = 0.32$, at $Q = 70$ ml/min. Insets in [(e)–(g)] show typical instantaneous finger shapes, marked as M1, M2, and M3. The shapes with asterisks were not recorded directly; instead, snapshots from the other daughter channel are used as representations of the shapes observed. Finger pressure P during the channel reopening experiments analogous to [(b)–(g)] as a function of scaled finger tip position (h) in the main channel X_1/W and (j) in the daughter channel X_2/W, respectively. The vertical dashed line in (h) denotes the start of the bifurcation region.

Fig. 7(e), or different modes of finger propagation, e.g., M1 and M2 in Fig. 7(f) or M2 and M3 in Fig. 7(g). We label these experiments according to the fingering modes observed in the daughter channels, e.g., M1-M2 corresponds to the reopening in Fig. 7(f).

In Fig. 7(h) we show the pressure data in the main channel and bifurcation region in five representative experiments at $Q = 70$ ml/min. The variability in the data is on the order of the experimental resolution. However, these small differences between experimental runs are sufficient to yield qualitatively different pressure traces downstream of the bifurcation region. This is shown in Fig. 7(j) using pressure traces from 10 experiments, with the remaining data omitted to avoid overloading the figure. Strikingly, a steady state of constant pressure was reached almost immediately for experiments labeled M1-M1, whereas for the experiments labeled M1-M2, it was only reached at the end of the daughter channel with a considerably lower value. Although the final pressures for M1-M1 and M2-M3 were similar, the M2-M3 pressure varied nonmonotonically, consistent with the evolution of the M3 finger shapes shown in Fig. 7(g). [Because of this transient reopening throughout the daughter channel, the experimental data for M2-M3 is not indicated in Fig. 7(a).]

These experiments clearly show that the modes of reopening of the daughter channels cannot always be predicted from knowledge of the finger patterns and pressure traces in the main channel. Beyond the multiplicity of long-term reopening scenarios, the multiple routes to steady-state propagation are also associated with a variety of characteristic time- and length scales for the decay of

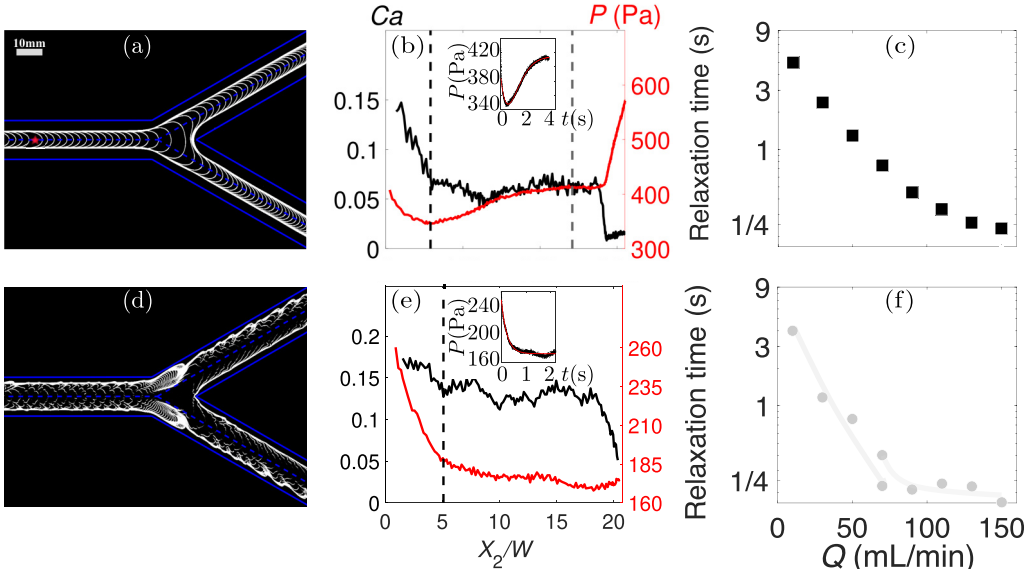

FIG. 8. Spatiotemporal composite image for (a) $Q = 70$ ml/min and $A_i = 0.91$ (0.89) in the main (daughter) channel and (d) $Q = 110$ ml/min and $A_i = 0.36$ (0.32) in the main (daughter) channel. The time interval between sequential contours is 0.017 s. [(b) and (e)] Capillary number Ca and finger pressure P as a function of scaled finger tip position in the daughter channel X_2/W for experiments in (a) and (d), respectively. Ca and P are approximately constant beyond the vertical dashed lines until the air finger reaches the end of one of the daughter channels [for (b), $\overline{\mathrm{Ca}}$ and $\overline{P}$ are reached at different locations, $X_2/W = 4.6$ and 15.5, respectively]. Insets show postbifurcation time evolution of the finger pressure P in the same experiments (black dots) and fits to the data (red lines) assuming (b) exponential and (e) modulated exponential decay to a constant pressure, see (1) and (2), respectively. [(c) and (f)] The relaxation time, T, obtained from fits such as in (b) and (e), as a function of the injection rate on a semilog scale obtained for experiments with (c) $A_i = 0.89$ and (f) $A_i = 0.32$ in the daughter channel. The squares and circles were obtained using (1) and (2), respectively. Lines in (f) are drawn to guide the eye.

transients. Although steady propagation was usually reached within the finite length of the daughter channels, the dynamics of the propagating finger would sometimes also exhibit long-lived transients during which the finger appeared to successively explore different modes of propagation known to exist in this system [31].

C. Steady-state recovery in the daughter channels

We have found that the transition distance of a steadily propagating finger postbifurcation can range from very short to longer than the length of the daughter channel in our experiment. This suggests that transient finger evolution during recovery may be more important to the reopening of an elastic network than steady states of propagation that may only be reached in sufficiently long channels, so we also study this transient evolution. The flow rate in each of the daughter channels is half of the injection flow rate, and the fingers propagate into channels that are marginally less stiff and therefore more collapsed than the main channel (see Sec. II). Moreover, the membrane is marginally less collapsed near the outer boundary at the inlet of the daughter channels due to the geometry of the network and the orientation of the imposed prestress, see Fig. 4(a).

As shown in Refs. [6,25,31], and discussed in Sec. III A, the reopening of straight channels depends crucially on whether viscous or elastic forces dominate. We therefore proceed to examine the recovery towards steady propagation in these two limits. Figure 8 compares finger propagation in

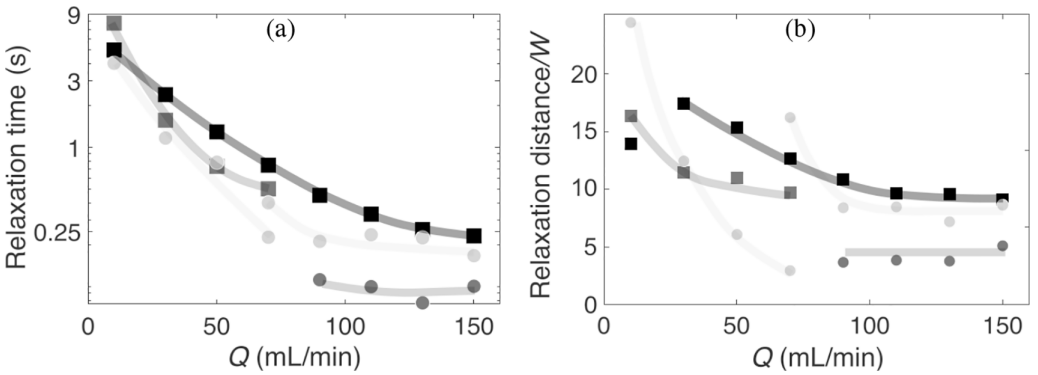

FIG. 9. Relaxation (a) time and (b) distance as a function of Q for $A_i = 0.91$ (0.88) (black markers), $A_i = 0.64$ (0.57) (gray markers) and $A_i = 0.36$ (0.32) (light gray markers) in the main (daughter) channel. As in Fig. 8, the squares and circles were obtained using (1) and (2), respectively, and lines are drawn to guide the eye.

the viscous regime ($Q = 70$ ml/min and $A_i = 0.91$, in the main channel, i.e., relatively low injection rate and low initial collapse) and in the elastic regime ($Q = 110$ ml/min and $A_i = 0.36$, in the main channel, i.e., relatively high injection rate and high initial collapse). In the viscous regime [Fig. 8(a)], the round-tipped symmetric finger in the main channel divides into similar daughter fingers at the bifurcation. In contrast, in the elastic regime [Fig. 8(d)], the finger front is flattened and feathered in the main channel and transitions to a different feathered pattern in the daughter channels. These regimes are associated with qualitatively different transient recovery in the daughter channels.

For the experiments in Fig. 8(a), the recovery of a steady state involves the monotonic decay of Ca to a constant value $\overline{\mathrm{Ca}}$, which is less than half of its value in the main channel [Fig. 8(b)]. However, P evolves nonmonotonically to reach its constant value $\overline{P}$. Thus, values for the average capillary number $\overline{\mathrm{Ca}}$ plotted in Figs. 6(a)–6(b) were obtained from experimental data by averaging Ca once it reached a constant value and errors were estimated as the standard deviation of the data within an experiment. In order to extract $\overline{P}$ from the time evolution of the pressure data, also shown in Fig. 8(b), we fitted an exponentially decaying function of the form

$$P(t) = C_1 \exp(-t/T)\cos(C_2 t + C_3) + \overline{P}, \tag{1}$$

where C_i ($i = \{1, 2, 3\}$) and T are fitting parameters. The fit is shown in the inset to Fig. 8(b). When fitting, we considered a range of possible $\overline{P}$ and selected the value which provided the best least-squares fit of a straight line to $\ln \frac{P(t)-\overline{P}}{\cos(C_2 t + C_3)}$. The fit also produced a characteristic timescale of transient decay T, which we refer to as the relaxation time. Figure 8(c) indicates that the relaxation time decreases monotonically with flow rate for viscous reopening.

For the experiments in Fig. 8(d), both Ca and P decay monotonically to their constant values $\overline{\mathrm{Ca}}$ and $\overline{\mathrm{Pa}}$, respectively, at approximately the same position $X_2/W = 5$ [Fig. 8(e)]. For this type of transients, exponentially decaying functions of the form

$$P(t) = C_0 \exp(-t/T) + \overline{P}, \tag{2}$$

were fitted to the time evolution of the pressure data in order to extract $\overline{P}$; see the inset to Fig. 8(e). As before, C_0 and T are fitting parameters. For this higher level of collapse, the relaxation time shown in Fig. 8(f) is discontinuous with flow rate. There are two groups of points corresponding to two peeling branches shown in Fig. 6(b). For data at smaller values of Q, we observe the same trend of monotonic decay as in Fig. 8(c). However, for the data on the second branch corresponding to the elastic reopening regime the relaxation time appears to saturate with increasing Q.

Figure 9(a) shows variation of the relaxation time with injection rate for all experiments performed with different levels of initial collapse. The interpretation of these results is complicated as the dominance of elastic over viscous forces can switch as the channel geometry changes (see Appendix B for the observations in the bifurcation region, for example), which in turn affects the length of transients. The shortest timescales of reopening, shown with dark gray circles in Fig. 9(a), are for fingers that adopt asymmetric shapes throughout the Y-channel, including in the bifurcation region, e.g., for experiments with $A_i = 0.64$ (0.57) in the main (daughter) channel. This is consistent with the fact that weakly asymmetric fingers are formed in the bifurcation (see Appendix B) and thus adjustment to steady asymmetric shapes is likely to be rapid.

A more practical description of the transient dynamics is in terms of a relaxation distance. We define it as the length of daughter channel required for the finger pressure to decay to within 2% of its value $\overline{P}$, a criterion which allows us to account for small fluctuations in $\overline{P}$. Results shown in Fig. 9(b) confirm the trends obtained for the relaxation time in Fig. 9(a), but the disconnection between data associated with different modes of propagation is amplified. For example, it is clear that at high initial collapse, the relaxation distance follows two separate trends with Q, resulting in an overall nonmonotonic variation with Q. At smaller values of Q, the length scale of decay routinely requires a long daughter channel exceeding 10 channel widths. The fact that the relaxation distance reaches a constant value for high Q suggests that it may be possible to build lower-dimensional models of elastic-walled networks based on the assumption of steady reopening in this regime, such as used in Refs. [33,34].

IV. CONCLUSION

In this paper we have presented a bench top model of the reopening of a liquid-filled, collapsed branching airway via the propagation of an air finger. Our model consists of a straight elastorigid Hele-Shaw channel which bifurcates into two daughter channels of similar geometry. We find that the influence of the channel bifurcation on the reopening dynamics depends significantly on the level of initial collapse and the rate of air injection. At lower levels of collapse, following the decay of transients, steady modes of finger propagation are recovered downstream of the bifurcation, which are similar to those in the main channel for suitably reduced flow rates. In this regime, the dynamics are insensitive to small differences in channel geometry between main and daughter channels.

However, at high levels of initial collapse, the finger dynamics becomes more complex and can exhibit sensitivity to small changes to the initial collapse, as evidenced by qualitatively different reopening processes in the main and daughter channels where initial collapse is only slightly larger. This sensitivity concurs with the results of Cuttle *et al.* [25] and Fontana [40] and in the bifurcating channel, it can lead to multiple reopening scenarios downstream of the bifurcation despite apparently identical fingers in the main channel.

We find that the recovery of a steady state downstream of the bifurcation is regulated by the same reopening mechanics that underpin finger propagation in straight elastorigid channels. At smaller flow rates and/or lower levels of initial collapse, it is dominated by the balance between viscous and surface tension forces—the viscous regime—and we find transients that persist for longer and over a large distance. As the flow rate and/or level of initial collapse increase, the system gradually transitions to the regime in which reopening is controlled by a balance between elastic and surface tension forces—the elastic regime. This is associated with an overall decrease in time scale and length scales of transients, but the route is complex because experiments can feature different reopening regimes in the main channel, bifurcation, and daughter channels for intermediate parameter values. In the elastic regime, the time- and length scales of the steady-state recovery are the shortest and reach a constant plateau.

A key assumption in all tractable models of multiphase flows in elastorigid networks is that their reopening is steady. Our experimental observations confirm that in channels of moderate length ($\lesssim$10 channel widths) this assumption is reasonable for a limited range of parameters in the elastic regime, where transients are relatively short lived. However, we also demonstrate complexity related

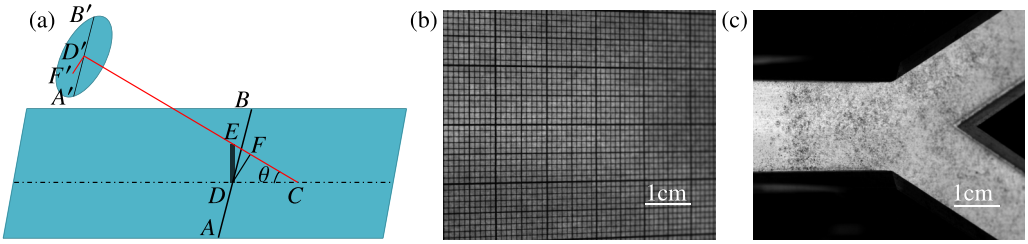

FIG. 10. (a) Schematic diagram of the principle behind detecting line deformations. Examples of (b) the calibration and (c) the reference image.

to dynamical sensitivity which is not accounted for in existing theoretical models, and thus our findings may be used to inform future modeling assumptions.

ACKNOWLEDGMENTS

The authors acknowledge Martin Quinn for his technical support. The work was funded by the EPSRC (Grant No. EP/R045364/1). H.L. thanks the China Scholarship Council (Grant No. 201906020184) support; F.B. acknowledges the Royal Society (Grant No. URF/R1/211730).

APPENDIX A: METHOD FOR RECONSTRUCTING VERTICAL DEFLECTION OF THE MEMBRANE

The method for reconstructing the vertical deflection of the membrane in our experiments relies on the method for reconstructing the vertical line displacement used by Ducloué *et al.* [6], Lister *et al.* [27], Pihler-Puzović *et al.* [41], and Cuttle *et al.* [25]. We start by considering a horizontal plane ABC, containing a point D that lies in the middle of the line AB; see Fig. 10(a). To reconstruct its position as it moves vertically to the point E, we place a camera at an angle θ with the horizontal. This implies that the image plane $A'B'D'F'$ is parallel with the plane $ABDF$, where FD' is at the angle θ with the plane ABC and DF forms an angle θ with the vertical displacement DE. Thus, it is possible to find the true displacement of the point D, DE, from the in-image displacement $D'F'$ using the conversion ratio $\mathcal{C} = DE/D'F' = DE/DF \cdot DF/D'F' = DF/D'F' \cdot 1/\cos\theta = \mathcal{S}/\cos\theta$, where $\mathcal{S}$ is a calibration factor, which in principle varies for different points on the line AB. However, as the width of the viewing area is much smaller than the camera-object distance in our experiments, we assume that the scale factor $\mathcal{S}$ stays constant along the line AB and obtain it by relating the number of the in-image pixels to the known length of the line AB. This allows us to calculate a vector of vertical displacements V_{VD} of points on the line AB from a vector of the corresponding in-image displacements V_{ID} using the relationship $V_{\mathrm{VD}} = V_{\mathrm{ID}} \cdot \mathcal{C}$.

To reconstruct the vertical deformation of the whole membrane, we needed to capture the deflection of points lying on many parallel lines which cover the region of interest. Before the channel was filled with liquid and collapsed to be subsequently inflated, a millimetric tracing paper was laid flat on the flat elastic wall and a calibration image was taken [see Fig. 10(b)]. For each of the parallel lines, the scale factor $\mathcal{S}$ and the angle θ were found from the calibration image and recorded in vectors $V_{\mathcal{S}}$ and V_θ, respectively. Thus, the conversion ratio vector $V_{\mathcal{C}} = \{V_{\mathcal{C}}^i\}$ for all lines was obtained using the formula $V_{\mathcal{C}}^i = V_{\mathcal{S}}^i/\cos(V_\theta^i)$. Then by knowing the in-image displacements M_{ID} of different points on the membrane, we could reconstruct the vertical deformation field M_{VD} using the matrix relationship

$$M_{\mathrm{VD}} = M_{\mathrm{ID}} \cdot V_{\mathcal{C}}. \tag{A1}$$

In our experiments, membrane deformations comprised both in-plane as well as out-of-plane displacements. Both types of displacements are typically reconstructed using stereo or three-

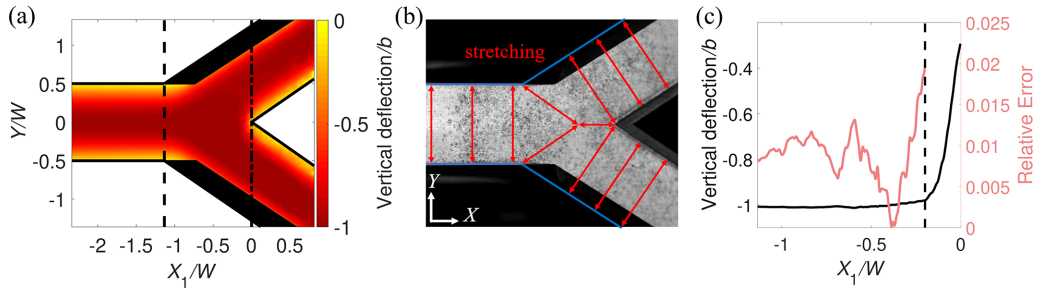

FIG. 11. (a) Membrane profile for $A_i = 0.33$ in the main channel before the start of air injection with color coding corresponding to the vertical deformation of the membrane scaled by b. Regions of the channel, where the vertical deformation could not be reconstructed, are black. Lines denote the boundaries of the channel (solid lines), the start of bifurcation region (vertical dashed line), and the apex of the bifurcation (vertical dash-dotted line). (b) Illustration of principal stretching directions in different regions of the Y-channel, whose boundaries are shown using (blue) solid lines. (c) Recorded membrane deformation in the longitudinal midplane of the bifurcation region (left axis) and the estimated relative error of this measurement (right axis). The vertical dashed line corresponds to $X_1/W = -0.2$, beyond which the relative error cannot be estimated because there is no opposite wall contact.

dimensional digital image correlation with two synchronized digital cameras or using single-camera stereodigital image correlation techniques with additional optical assistance [42]. These techniques track three-dimensional positions of random particles, deposited on the deforming object. We also traced a random speckle pattern on the elastic membrane created by sprinkling food powder onto it while it was still flat, as shown in the reference image Fig. 10(c). However, we chose to neglect the deformations due to in-plane stretching, assuming that the membranes predominantly deformed through vertical displacement. This allowed us to employ one camera as in experiments with a single line and apply a two-dimensional digital image correlation technique (2D DIC) to obtain the in-image displacements M_{ID} of the speckle pattern. We used the 2D DIC method available as an open-source MATLAB software Ncorr v1.2 [43], which employs a sum-squared difference correlation criteria [44] to match the particles before and after the deformation and the B-spline interpolation [45] to enhance the method for finding the displacement field to subpixel accuracy. We found that imaging the membrane using a CMOS camera (Teledyne Dalsa CR-GM00-H1400, resolution 1400×1024 pixels) at 1 frame per second during the collapse and at 60 frames per second during the reopening experiments, respectively, was sufficient to reproduce reliable in-image displacement measurements which could then be used to extract the vertical deformations using (A1).

When reconstructing the vertical displacements M_{VD} of the membrane, e.g., in Fig. 11(a), we only used the in-image displacements in the flow direction [marked as X in the image Fig. 11(b)], and while the horizontal in-plane stretching of the membrane was much smaller than its vertical displacement, it was nevertheless the primary error source for the proposed method over the majority of the channel area. The predominant direction of the stretching, schematically shown with red double arrows in Fig. 11(b), was different in the main channel, the bifurcation region, and the daughter channels. In the main channel, the reconstructed deflections were not affected significantly by the in-plane displacement, which was mostly confined to the Y direction. However, in the bifurcation region and the daughter channels, the stretching contributed significantly to the X-directional in-image displacements. This was especially true at the apex of the bifurcation, where the direction of stretching coincided exactly with the X direction. Conversely, in the main channel the error was expected to be the largest near the side boundaries, which are not captured precisely by the camera due to a small unavoidable misalignment between the channel and the metal frame clamping the elastic membrane.

In order to quantify these errors of the measurement method, we utilized the deformation results obtained for the cross-sectional area of $A_i = 0.33$ in the main channel, when the opposite wall contact occurred centrally in all parts of channel [see Fig. 11(a)]. By assuming the real vertical displacements along the central lines and the boundaries of the main or daughter channels to be -0.5 and 0 mm, respectively, we extracted the relative errors on the vertical displacement in these regions by comparing them to the depth of undeformed channel, as done in the bifurcation region in Fig. 11(c). This yields errors of up to 1.3% and 3.9% on the deflection along the centerlines of the main and the daughter channels, respectively. The relative error near the boundaries of the channels increases to 7% and 16.7%, respectively. The greatest relative error of 33% was estimated at the bifurcation apex. However, we are primarily interested in the vertical displacements of the channel centerline in the region of $X_1/W \leqslant -0.2$ (as discussed in Appendix B), where the relative error on the displacement is less than 2% in Fig. 11(c). For $-0.2 \leqslant X_1/W < 0$ in Fig. 11(c), we could not estimate the errors using the arguments above, as this region corresponds to where the membrane adjusts its deformation from the opposite wall contact to being clamped at the apex.

APPENDIX B: REOPENING OF THE BIFURCATION REGION

Experimental observations in the bifurcation region of the channel also support the conclusion that reopening in different parts of the Y-channel can be dominated by different forces, which in turn affects the recovery of the steady state in the daughter channels. To demonstrate this convincingly, we focus on experiments performed at a modest value of the flow rate $Q = 10$ ml/min so that both main and daughter channels can reopen steadily for all levels of initial collapse. The height of the collapsed channel is lower in the bifurcation region compared with the main channel [see Fig. 4(a)], and its width varies linearly, which perturbs the incoming fingers and precludes their steady propagation within the bifurcation region. Different reopening regimes within the same experiment are thus a consequence of the changing geometry, which leads to altered constitutive relationships between pressure and cross-sectional area of the channels.

Figure 12 shows sequences of finger outlines in top-view (left column) and the corresponding sheet profiles along the longitudinal vertical midplane of the main channel (black lines, right column) for five levels of initial collapse, $0.36 \leqslant A_i \leqslant 0.91$ in the main channel. In the side-view visualization, the position of the propagating finger tip is indicated by vertical red lines. All fingers shown in Fig. 12 have rounded tips in the main channel, which is indicative of viscous reopening. Yet their shapes in the bifurcation region at larger levels of initial collapse [Figs. 12(g) and 12(i)] are typical of elastic reopening. For $0.64 \leqslant A_i \leqslant 0.91$, the moderate initial collapse means that the volume of fluid displaced in front of the finger as it propagates into the bifurcation region is sufficient to inflate this domain significantly beyond the level of inflation in the main channel [Figs. 12(b), 12(d) and 12(f)]. This excess inflation is enhanced by the slowing of the finger as it approaches the apex of the bifurcation. Thus, the fingers retain the round tip characteristic of viscous reopening through the bifurcation region, until the interface flattens to accommodate tip-splitting caused by the forking of the channel [Figs. 12(a), 12(c) and 12(e)]. However, as A_i is reduced, membrane profiles that correspond to fingers still propagating in the main channel get steeper, indicating a reduction in the length of the liquid wedge. When the level of initial collapse is reduced to $A_i = 0.49$ and then further to 0.36 [Figs. 12(g)–12(j)], there is initial opposite wall contact between the top elastic sheet and the bottom boundary in the bifurcation region. This further reduces the volume of fluid during the reopening experiments, resulting in a minimal liquid wedge ahead of the finger which can no longer promote the inflation of the channel in the bifurcation region. As the finger advances into the bifurcation region with the elastic sheet in this limiting configuration [Figs. 12(h) and 12(j)] the finger tip flattens and its speed decreases slightly to accommodate the widening of the finger [Figs. 12(g) and 12(i)].

Figure 13 summarizes the transition from viscous to elastic reopening depicted in Fig. 12. The sheet deflection at the finger tip shown in Fig. 13(a) increases within the bifurcation region

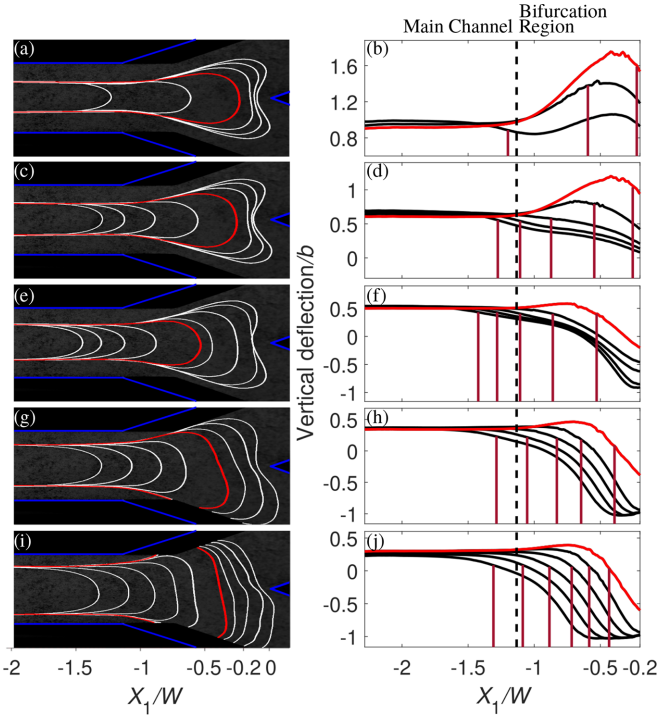

FIG. 12. Finger shapes (left column), instantaneous membrane deformations in the longitudinal midplane of the main channel (black lines in the right column) and the corresponding positions of the finger tip (red vertical lines in the right column) for [(a) and (b)] $A_i = 0.91$, [(c) and (d)] $A_i = 0.75$, [(e) and (f)] $A_i = 0.64$, [(g) and (h)] $A_i = 0.49$, and [(i) and (j)] $A_i = 0.36$ and $Q = 10$ ml/min (all levels of initial collapse cited based on the main channel A_i). Note that there are more finger contours than corresponding membrane deformations due to limited resolution of the membrane deformation reconstruction method near the apex of the bifurcation ($-0.2 < X_1/W < 0$) (see Appendix A); the last contours and membrane deformations that correspond to each other are shown in red. Time intervals between sequential contours or membrane deformations are [(a) and (b)] 0.08 s, [(c) and (d)] 0.04 s, [(e) and (f)] 0.08 s and then 0.3 s beyond the red contour, [(g) and (h)] 0.24 s and then 0.43 s beyond the red contour, and [(i) and (j)] 0.36 s and then 0.4 s beyond the red contour, respectively. The blue lines in the left column mark boundaries of the Y-channel and the dashed line in the right column marks the start of the bifurcation region.

indicating enhanced inflation relative to the main channel for $0.64 \leqslant A_i \leqslant 0.91$. In contrast, a marginal decrease indicating deflation relative to the main channel occurs for $0.36 \leqslant A_i \leqslant 0.49$.

The plots of Ca and P as a function of scaled finger tip position X_1/W for high, medium, and low collapse [Figs. 13(b) and 13(c)] indicate that the geometry of the bifurcation region affects the finger while it is still propagating in the main channel. The distance at which departure from steady propagation occurs increases with decreasing level of initial collapse because of the lengthening wedge of recirculated liquid ahead the finger. Pressure and capillary number traces also reflect the qualitative difference in the reopening of the bifurcation region between modest (black and gray curves) and high initial collapse (light gray curve). For low to moderate initial collapse, Ca increases and P decreases as the finger approaches the bifurcation region. This is because resistance to propagation is reduced in the widening channel which lowers viscous and elastic forces. Therefore, once the finger enters the bifurcation region and begins to widen, Ca decreases to satisfy air mass conservation. The wider channel means that lower pressure is required for inflation and thus pressure continues to decrease. In contrast, for $A_i = 0.36$ in the main channel, the cross-sectional area of the

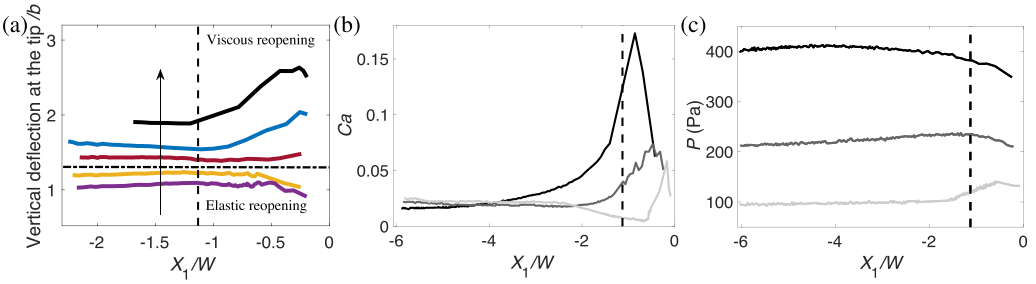

FIG. 13. (a) The membrane deflection at the finger tip, normalized by the channel depth b, as a function of scaled finger tip position X_1/W for $A_i = 0.36$, 0.49, 0.64, 0.75, and 0.91 in the main channel (increasing in the direction of the arrow) and $Q = 10$ ml/min. The horizontal dashed-dotted line is added to stress the change in the behavior of membrane deflection at the finger tip. (b) Ca and (c) P as a function of scaled finger tip position X_1/W for different A_i and fixed $Q = 10$ ml/min. The black, gray and light gray lines correspond to the experimental data for $A_i = 0.91$, 0.64, and 0.36 in the main channel, respectively. The vertical dashed lines mark the start of the bifurcation region.

channel does not change significantly as the finger enters the bifurcation region because the channel is highly collapsed. Once opposite wall contact occurs, a considerable increase in the transmural pressure is required to alter the channel cross section [see Fig. 4(c)]. Thus, the finger quickly widens on entering the bifurcation region but its thickness hardly changes, which results in a weakly decreasing Ca under the constant volumetric flow rate constraint. The finger eventually inverts the concave elastic sheet in a snappinglike manner at a threshold pressure. Once the sheet has inflated, P and Ca follow the trends observed for lower initial collapse.

[1] A. M. Alencar, S. P. Arold, S. V. Buldyrev, A. Majumdar, D. Stamenović, H. E. Stanley, and B. Suki, Dynamic instabilities in the inflating lung, Nature (Lond.) **417**, 809 (2002).

[2] F. Bosetti, Z. S. Galis, M. S. Bynoe, M. Charette, M. J. Cipolla, G. J. del Zoppo, D. Gould, T. S. Hatsukami, T. L. Z. Jones, J. I. Koenig, G. A. Lutty, C. Maric-Bilkan, T. Stevens, H. E. Tolunay, and W. Koroshetz, "Small blood vessels: Big health problems?": Scientific recommendations of the National institutes of Health workshop, J. Am. Heart Assoc. **5**, e004389 (2016).

[3] A. B. te Pas, P. G. Davis, S. B. Hooper, and C. J. Morley, From liquid to air: Breathing after birth, J. Pediatr. **152**, 607 (2008).

[4] H. A. Stone, Tuned-in flow control, Nat. Phys. **5**, 178 (2009).

[5] J. Alvarado, J. Comtet, E. deLangre, and A. E. Hosoi, Nonlinear flow response of soft hair beds, Nat. Phys. **13**, 1014 (2017).

[6] L. Ducloué, A. L. Hazel, A. B. Thompson, and A. Juel, Reopening modes of a collapsed elasto-rigid channel, J. Fluid Mech. **819**, 121 (2017).

[7] D. P. A. Juel and M. Heil, Instabilities in blistering, Annu. Rev. Fluid Mech. **50**, 691 (2018).

[8] M. Heil and A. L. Hazel, Flow in flexible/collapsible tubes, in *Fluid-Structure Interactions in Low-Reynolds-Number Flows* (Royal Society of Chemistry, Cambridge, UK, 2015).

[9] C. N. Baroud, S. Tsikata, and M. Heil, The propagation of low-viscosity fingers into fluid-filled branching networks, J. Fluid Mech. **546**, 285 (2006).

[10] A. T. S. Cerdeira, J. B. L. M. Campos, J. M. Miranda, and J. D. P. Araújo, Review on microbubbles and microdroplets flowing through microfluidic geometrical elements, Micromachines **11**, 201 (2020).

[11] A. Merlo, M. Berg, P. Duru, F. Risso, Y. Davita, and S. Lorthois, A few upstream bifurcations drive the spatial distribution of red blood cells in model microfluidic networks, Soft Matter **18**, 1463 (2022).

[12] A. L. Hazel and M. Heil, Three-dimensional airway reopening: The steady propagation of a semi-infinite bubble into a buckled elastic tube, J. Fluid Mech. **478**, 47 (2003).
[13] D. P. Gaver, D. Halpern, O. E. Jensen, and J. B. Grotberg, The steady motion of a semi-infinite bubble through a flexible-walled channel, J. Fluid Mech. **319**, 25 (1996).
[14] O. E. Jensen, M. K. Horsburgh, D. Halpern, and D. P. Gaver, The steady propagation of a bubble in a flexible-walled channel: Asymptotic and computational models, Phys. Fluids **14**, 443 (2002).
[15] D. Halpern, S. Naire, O. E. Jensen, and D. P. Gaver, Unsteady bubble propagation in a flexible channel: Predictions of a viscous stick-slip instability, J. Fluid Mech. **528**, 53 (1999).
[16] A. Heap and A. Juel, Anomalous bubble propagation in elastic tubes, Phys. Fluids **20**, 081702 (2008).
[17] D. P. Gaver, R. W. Samsel, and J. Solway, Effects of surface tension and viscosity on airway reopening, J. Appl. Physiol. **69**, 74 (1990).
[18] M. L. Perun and D. P. Gaver, An experimental model investigation of the opening of a collapsed untethered pulmonary airway, Trans. ASME: J. Biomech. Eng. **117**, 245 (1995).
[19] M. L. Perun and D. P. Gaver, Interaction between airway lining fluid forces and parenchymal tethering during pulmonary airway reopening, J. Appl. Physiol. **79**, 1717 (1995).
[20] A. L. Hazel and M. Heil, The influence of gravity on the steady propagation of a semi-infinite bubble into a flexible channel, Phys. Fluids **20**, 092109 (2008).
[21] P. G. Saffman and G. Taylor, The penetration of a fluid into a porous medium or Hele-Shaw cell containing a more viscous liquid, Proc. R. Soc. Lond. A **245**, 312 (1958).
[22] Y. Couder, Viscous fingering as an archetype for growth patterns, in *Perspectives in Fluid Mechanics: A Collective Introduction to Current Research*, edited by G. K. Batchelor, H. K. Moffat, and M. G. Worster (Cambridge University Press, Cambridge, UK, 2000), pp. 53–104.
[23] A. B. Thompson, A. Juel, and A. L. Hazel, Multiple finger propagation modes in Hele-Shaw channels of variable depth, J. Fluid Mech. **746**, 123 (2014).
[24] A. Franco-Gómez, A. B. Thompson, A. L. Hazel, and A. Juel, Sensitivity of Saffman–Taylor fingers to channel-depth perturbations, J. Fluid Mech. **794**, 343 (2016).
[25] C. Cuttle, D. Pihler-Puzović, and A. Juel, Dynamics of front propagation in a compliant channel, J. Fluid Mech. **886**, A20 (2020).
[26] A. D. McEwan and G. I. Taylor, The peeling of a flexible strip attached by a viscous adhesive, J. Fluid Mech. **26**, 1 (1966).
[27] J. R. Lister, G. G. Peng, and J. A. Neufeld, Viscous Control of Peeling an Elastic Sheet by Bending and Pulling, Phys. Rev. Lett. **111**, 154501 (2013).
[28] D. Pihler-Puzović, P. Illien, M. Heil, and A. Juel, Suppression of Complex Fingerlike Patterns at the Interface Between Air and a Viscous Fluid by Elastic Membranes, Phys. Rev. Lett. **108**, 074502 (2012).
[29] L. Ducloué, A. L. Hazel, D. Pihler-Puzović, and A. Juel, Viscous fingering and dendritic growth under an elastic membrane, J. Fluid Mech. **826**, R2 (2017).
[30] E. Lajeunesse and Y. Couder, On the tip-splitting instability of viscous fingers, J. Fluid Mech. **419**, 125 (2000).
[31] J. V. Fontana, A. Juel, N. Bergemann, M. Heil, and A. L. Hazel, Modelling finger propagation in elasto-rigid channels, J. Fluid Mech. **916**, A27 (2021).
[32] J. V. Fontana, C. Cuttle, D. Pihler-Puzović, A. L. Hazel, and A. Juel, Peeling fingers in a compliant channel (unpublished).
[33] P. S. Stewart and O. E. Jensen, Patterns of recruitment and injury in a heterogeneous airway network model, J. R. Soc. Interf. **12**, 20150523 (2015).
[34] J. F. Louf, F. Kratz, and S. S. Datta, Elastocapillary network model of inhalation, Phys. Rev. Res. **2**, 043382 (2020).
[35] E. Yamaguchi, M. J. Giannetti, M. J. V. Houten, O. Forouzan, S. S. Shevkoplyas, and D. P. Gaver, The unusual symmetric reopening effect induced by pulmonary surfactant, J. Appl. Physiol. **116**, 635 (2014).
[36] K. J. Cassidy, N. Gavriely, and J. B. Grotberg, Liquid plug flow in straight and bifurcating tubes, J. Biomech. Eng. **123**, 580 (2001).
[37] Y. Song, M. Baudoin, P. Manneville, and C. N. Baroud, The air–liquid flow in a microfluidic airway tree, Med. Eng. Phys. **33**, 849 (2011).

[38] M. Baudoin, Y. Song, P. Manneville, and C. N. Baroud, Airway reopening through catastrophic events in a hierarchical network, Proc. Natl. Acad. Sci. USA **110**, 859 (2013).
[39] B. Audoly and Y. Pomeau, *Elasticty and Geometry: From Hair Curls to the Nonlinear Response of Shells* (Oxford University Press, Oxford, 2008).
[40] J. V. Fontana, Propagation of bubbles in collapsed Elasto-rigid Hele-Shaw channels, Ph.D. thesis, The University of Manchester, 2021.
[41] D. Pihler-Puzović, A. Juel, G. G. Peng, J. R. Lister, and M. Heil, Displacement flows under elastic membranes. Part 1. Experiments and direct numerical simulations, J. Fluid Mech. **784**, 487 (2015).
[42] B. Pan, L. Yu, and Q. Zhang, Review of single-camera stereo-digital image correlation techniques for full-field 3D shape and deformation measurement, Sci. China Technol. Sci. **61**, 2 (2018).
[43] The software is available at http://www.ncorr.com.
[44] W. Tong, An evaluation of digital image correlation criteria for strain mapping applications, Strain **41**, 167 (2005).
[45] H. W. Schreier, J. R. Braasch, and M. A. Sutton, Systematic errors in digital image correlation caused by intensity interpolation, Opt. Eng. **39**, 2915 (2000).